AIAA Journal
Vol. 47, No. 10, October 2009

Continuum Aeroelastic Model for a Folding-Wing Configuration

Sebastian Liska* and Earl H. Dowell†
Duke University, Durham, North Carolina 27708

DOI: 10.2514/1.40475

An aeroelastic model and analytical solution methodology are developed to find the flutter solutions for the continuous representation of a two-segment uniform folding wing. The model is developed such that different parameters can be easily modified to examine changes in the flutter solutions. Of these parameters, the fold angle between the inboard and outboard wing segments is of particular interest for understanding the fundamental aeroelastic behavior of folding wings. The results are presented as the evolution of the aeroelastic frequencies and damping with respect to the freestream velocity. This enables the determination of flutter speeds and modes. Three aerodynamic models of increasing sophistication are considered, which underscore the sensitivity of the flutter solution to unsteady effects. The capabilities of the aeroelastic analysis are demonstrated for a test case in which the flutter speed is plotted versus fold angle for three aerodynamic models.

Nomenclature

a = axis of rotation at $\frac{1}{2}ac$ from midchord (positive aft)
$C(\bar{\eta})$ = Theodorsen function
c = chord, m
$D(\bar{\eta})$ = generalized or complex Theodorsen function
E = Young's modulus, Pa
G = shear modulus, Pa
h = vertical displacement of elastic axis (positive down), m
h_U = vertical displacement of elastic axis perpendicular to U_∞ and span (positive down), m
I_{xx} = area moment of inertia the cross-sectional x axis $(\frac{1}{12}cw^3)$, m^4
I_y = mass moment of inertia per unit span $(\frac{1}{12}\rho wc^3 + \lambda_P x_P^2)$, kg · m
J = Saint-Venant's torsion constant $(\frac{1}{3}cw^3)$, m^4
$\bar{L}$ = lift per unit span, N/m
ℓ = span, m
$\bar{M}$ = moment per unit span, N · m/m
m = wing spanwise density $(\rho wc + \lambda_P)$, kg/m
S_y = static mass moment per unit span $(\lambda_P x_P)$, kg
T = kinetic energy, J
t = time, s
U = potential energy, J
U_∞ = freestream velocity, m/s
W = virtual work, J
w = thickness, m
xyz = Cartesian coordinates
x_P = distance of spanwise line mass from elastic axis (positive aft), m
α = angle of attack, rad
$\delta()$ = variational operator
η = temporal eigenvalue, Hz
$\bar{\eta}$ = reduced temporal eigenvalue $(\eta c/2U_\infty)$
λ = spatial eigenvalue, 1/m
$\hat{\lambda}$ = spatial eigenvalue squared (λ^2), 1/m^2
λ_P = spanwise line mass density, kg/m
ρ = uniform wing density, kg/m^3
ρ_∞ = freestream density, kg/m^3
ϕ = twist about the elastic axis (positive along the y axis), rad
ψ = fold angle, rad
$\cdot$ = $\partial/\partial t$
$'$ = $\partial/\partial y$

Subscripts

F = uniform wing
i, j, k = matrix/vector indices
P = spanwise line mass
S = torsional spring
1 = inboard wing
2 = outboard wing

I. Introduction

Recent studies in aircraft design suggest that wing configurations with significant morphing capability will lead to the next generation of multitask aircraft [1,2]. Currently, there are several research efforts focused on developing wings capable of dramatically changing their span during flight [3–5]. To meet this challenge, effective theoretical and computational methods are developed in this paper to model the coupled structural and aerodynamic behavior of a *folding-wing configuration*. Exact solutions are obtained for a linear continuum model of a two-segment folding wing, from which both divergence and flutter aeroelastic instabilities are identified. Structures experiencing either of the aforementioned instabilities could suffer significant damage, if not failure, due to large-amplitude oscillations.

A continuum model with exact solutions provides a framework to understand the fundamental physics of folding-wing configurations. The solution procedure is *exact* in that it solves the differential equations of motion directly and does not rely on either the spatial discretization of finite element or modal analysis. Thus, the present solution provides benchmark solutions for any discretized method of solution and it is the folding-wing analog to the well-known Goland wing solution for a single-element beam-wing analysis. The solution procedure is also exact in that it solves for the true aeroelastic eigenvalues at all flow speeds, unlike classical flutter solution methods, which are only exact at the flutter speed per se.

The dynamic model is developed using Hamilton's principle. The aerodynamic forces are modeled using strip theory for thin airfoils [6]. Following this assumption, three linear subsonic aerodynamic models are considered: steady, quasi-steady, and full unsteady. The complexity of the solutions and numerical efforts depend on the sophistication of the model. Therefore, it is worthwhile to investigate the fidelity of the steady and quasi-steady solutions in relation to the unsteady solutions.

Received 18 August 2008; revision received 14 May 2009; accepted for publication 4 July 2009.

[*] Research Assistant, Department of Mechanical Engineering and Materials Science. Student Member AIAA.

[†] William Holland Hall Professor, Department of Mechanical Engineering and Materials Science. Honorary Fellow AIAA.

II. Development of Equations of Motion and Boundary Conditions

The structural model consists of two wing segments. The inboard wing is clamped at its root, and the outboard wing is connected to the inboard wing through a single hinge. Each wing segment is modeled as a uniform flat plate with a superimposed spanwise line mass at a prescribed chordwise location. The presently developed equations of motion and boundary conditions can also be applied to uniform wing segments for which the elastic axis (EA) does not coincide with the half-chord. Aerodynamic considerations for an EA not coincident with the half-chord are discussed in subsequent sections. Note that a point mass added at the outboard segment tip would contribute to the outer wing's boundary conditions. Indeed, a point mass at any spanwise location could be taken into account, but at the cost of additional complexity in the analysis.

A. Structural Model

The current derivation models the two wing segments as flat rectangular plates of equal chord with uniform material properties. Each flat plate is considered to be *thin*, meaning that the thickness is much smaller than the chord and length of any given wing segment. Linear elastic beam theory is used to describe the dynamic behavior of the wing segments. The EA is located at the half-chord. Even though each plate has uniform material properties, a uniform line mass along the span has been added to separate the chordwise center of mass (CM) from the EA. This line mass is located x_P aft of the EA. The aerodynamic center (AC) is located a quarter-chord distance fore of the EA. The motion of the CM of each wing segment along the chordwise direction is neglected. The vertical deflection h_i and the twist ϕ_i are functions of y_i and t only (see Fig. 1). A single one-degree-of-freedom hinge with a linear torsional spring constant along the entire chord connects the inboard and outboard wings. For an undeflected configuration, the wing segments are at a fixed fold angle ψ with respect to each other; an undeflected torsional spring corresponds to this fold angle.

The coordinate systems used are depicted in Fig. 1. The origins of the coordinate systems for both the inboard ($x_1y_1z_1$) and outboard ($x_2y_2z_2$) wings are along the EA, corresponding to the half-chord. Each segment has two degrees of freedom: h_i and ϕ_i. The vertical displacement h_i is measured from the EA and is positive downward. The twist about the EA ϕ_i is measured along the positive y_i axis. The origin of $x_2y_2z_2$ is located at $x_1 = 0$, $y_1 = \ell_1$, and $z_1 = h_1(\ell_1, t)$, where x_2 is parallel to the chord of the tip of the inboard wing. By definition, $\phi_2(0, t) = h_2(0, t) = 0$. Note that $x_1y_1z_1$ is fixed with respect to inertial space, as opposed to $x_2y_2z_2$.

The structural dynamics of each wing segment are modeled by Euler–Bernoulli beam theory. Forces due to gravity are considered negligible and are thus excluded for the analysis. The expressions for the kinetic and potential energies are included in Appendix A.

B. Aerodynamic Model

Steady, quasi-steady, and full unsteady linear aerodynamic models are considered for incompressible subsonic flows. The aeroelastic models use strip theory, which assumes that the lift on each wing segment is proportional to the geometric angle of attack and is independent of all other spanwise locations [6]. Each of these spanwise strips uses known results for two-dimensional flow (i.e., for an infinite span airfoil) and applies them to finite span airfoils. According to thin airfoil theory, the aerodynamic center is located at the quarter-chord from the leading edge. The parameter a is defined positive aft from the midchord, where $\frac{1}{2}ac$ is the distance from the midchord to the EA.

Of particular importance for implementing all three models is the proper definition of the angle of attack or twist α and the distance of the EA perpendicular to the flow h_U. By convention, the flow velocity U_∞ is along the x axis, and h_U is positive downward, as shown in Fig. 2.

Both α_1 and $h_{U,1}$ of the inboard wing can be readily obtained and should be obvious after neglecting higher-order terms in ϕ_1 and h_1:

$$\alpha_1 = \phi_1(y_1, t) \tag{1}$$

$$h_{U,1} = h_1(y_1, t) \tag{2}$$

Less obvious, but still intuitive, are α_2 and $h_{U,2}$ for the outboard wing:

$$\alpha_2 = \phi_1(\ell_1, t)\cos\psi + \phi_2(y_2, t) \tag{3}$$

$$h_{U,2} = h_1(\ell_1, t)\cos\psi + h_2(y_2, t) \tag{4}$$

The expressions used for lift and moment are limited to the Laplace domain, represented by the complex η plane. The extension of these aerodynamic theories to the time domain is beyond the scope of this paper.

1. Steady Model

A steady aerodynamic model is the simplest model considered in this paper. This model serves as a useful reference to interpret the solutions from the quasi-steady and full unsteady models. For this steady model, the lift per unit span $\bar{L}$ depends linearly on the angle of attack, and the aerodynamic moment per unit span $\bar{M}$ is due to the lift applied at the quarter-chord [7,8]:

$$\bar{L} = \pi c \rho_\infty U_\infty^2 \alpha \tag{5}$$

$$\bar{M} = \tfrac{1}{2}c^2 \rho_\infty U_\infty^2 (\tfrac{1}{2} + a)\alpha \tag{6}$$

It is worth noting that the preceding expressions do not contain a time derivative, thus making it a *steady* model.

2. Quasi-Steady Model

The quasi-steady model considered is similar to the steady model, but it accounts for the effects of the EA velocity on the instantaneous inclination of the airfoil [7,8]. Hence, the steady angle of attack α is replaced with the effective angle of attack $\alpha + (\dot{h}/U_\infty)$.

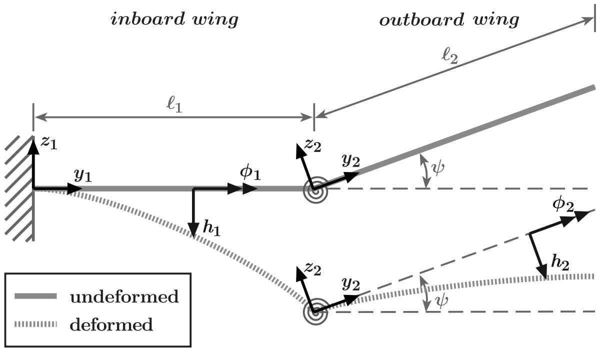

Fig. 1 Coordinates used in discussion of a two-segment folding wing. The curves represent the EA of the wing.

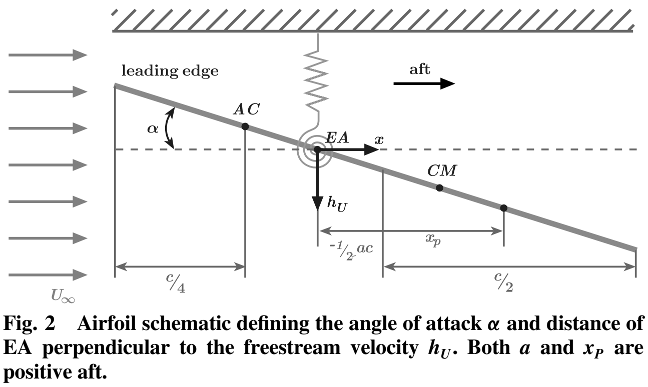

Fig. 2 Airfoil schematic defining the angle of attack α and distance of EA perpendicular to the freestream velocity h_U. Both a and x_P are positive aft.

3. Unsteady Model

The most sophisticated model considered is an unsteady aerodynamic model following a generalization of Theodorsen theory for damped oscillations. One of the key resulting features of the theory is the generalized Theodorsen function, which depends on the motion's frequency and damping and describes the magnitude and phase of circulatory effects in unsteady aerodynamics. The expressions for the resulting lift and aerodynamic moment in the Laplace domain are equivalent to those of the classical Theodorsen theory, with the exception that the Theodorsen function $C(\bar{\eta})$ is replaced by the generalized or complex Theodorsen function $D(\bar{\eta})$ [9,10]:

$$D(\bar{\eta}) = \frac{K_1(\bar{\eta})}{K_1(\bar{\eta}) + K_0(\bar{\eta})} \tag{7}$$

where K_0 and K_1 are the modified Bessel functions of the second kind, and $\bar{\eta}$ is the reduced temporal eigenvalue. The expression for the generalized Theodorsen function is defined in the entire complex plane, except on the branch cut along the negative real axis and the branch point at the origin. For the special case of $\eta = i\Im(\eta)$, we recover the Theodorsen function [11]:

$$D(i\Im(\bar{\eta})) = C(\Im(\bar{\eta})) = \frac{H_1^{(2)}(\Im(\bar{\eta}))}{H_1^{(2)}(\Im(\bar{\eta})) + iH_0^{(2)}(\Im(\bar{\eta}))} \tag{8}$$

where $H_1^{(2)}$ and $H_0^{(2)}$ are Hankel functions of the second kind.

The general expressions for lift and moment per unit span follow [7,8]:

$$\begin{aligned}\bar{L} &= \tfrac{1}{4}\pi c^2 \rho_\infty (\ddot{h}_U + U_\infty \dot{\alpha} - \tfrac{1}{2} c a \ddot{\alpha}) \\ &\quad + \pi c \rho_\infty U_\infty D(\bar{\eta})[\dot{h}_U + U_\infty \alpha + \tfrac{1}{2} c(\tfrac{1}{2} - a)\dot{\alpha}]\end{aligned} \tag{9}$$

$$\begin{aligned}\bar{M} &= \tfrac{1}{8}\pi c^3 \rho_\infty [a\ddot{h}_U - U_\infty(\tfrac{1}{2} - a)\dot{\alpha} - \tfrac{1}{2} c(\tfrac{1}{8} + a^2)\ddot{\alpha}] \\ &\quad + \tfrac{1}{2}\pi c^2 \rho_\infty U_\infty (\tfrac{1}{2} + a) D(\bar{\eta})[\dot{h}_U + U_\infty \alpha + \tfrac{1}{2} c(\tfrac{1}{2} - a)\dot{\alpha}]\end{aligned} \tag{10}$$

In general, the EA is located $\frac{1}{2}ac$ aft of the midchord, but for the model presently analyzed, the EA is located at the midchord (i.e., $a = 0$).

C. Equations of Motion and Boundary Conditions

The equations of motion are derived from Hamilton's principle and the known boundary conditions (see Table 1):

$$\int_{t_1}^{t_2} (\delta T - \delta U + \delta W)\,\mathrm{d}t = 0 \tag{11}$$

Note that all of the aerodynamics are contained in the virtual work δW. The virtual work depends only on the aerodynamics because there is no structural damping.

The terms δT and δU in Eq. (11) can be obtained by applying the δ operator directly to the kinetic and potential energy expressions presented in Appendix A. The expression for the virtual work due to aerodynamic forces requires kinematic considerations to be expressed in terms of the known lift and moment per unit span, particularly for the outboard wing:

$$\begin{aligned}\delta W &= \int_0^{\ell_1} \bar{M}_1 \delta\phi_1(y_1, t) - \bar{L}_1 \delta h_1(y_1, t)\,\mathrm{d}y_1 \\ &\quad + \int_0^{\ell_2} \bar{M}_2[\delta\phi_1(\ell_1, t)\cos\psi + \delta\phi_2(y_2, t)] \\ &\quad - \bar{L}_2[\delta h_1(\ell_1, t)\cos\psi + \delta h_2(y_2, t)]\,\mathrm{d}y_2\end{aligned} \tag{12}$$

1. Equations of Motion

$$S_y\ddot{\phi}_1(y_1, t) + m\ddot{h}_1(y_1, t) + EI_{xx}h_1^{(iv)}(y_1, t) + \bar{L}_1(y_1, t) = 0 \tag{13}$$

$$\begin{aligned}&S_y[\ddot{\phi}_1(\ell_1, t)\cos\psi + \ddot{\phi}_2(y_2, t)] + m[\ddot{h}_1(\ell_1, t)\cos\psi + \ddot{h}_2(y_2, t)] \\ &\quad + EI_{xx}h_2^{(iv)}(y_2, t) + \bar{L}_2(y_2, t) = 0\end{aligned} \tag{14}$$

$$I_y\ddot{\phi}_1(y_1, t) + S_y\ddot{h}_1(y_1, t) - GJ\phi_1''(y_1, t) - \bar{M}_1(y_1, t) = 0 \tag{15}$$

$$\begin{aligned}&I_y[\ddot{\phi}_1(\ell_1, t)\cos\psi + \ddot{\phi}_2(y_2, t)] + S_y[\ddot{h}_1(\ell_1, t)\cos\psi + \ddot{h}_2(y_2, t)] \\ &\quad - GJ\phi_2''(y_2, t) - \bar{M}_2(y_2, t) = 0\end{aligned} \tag{16}$$

2. Boundary Conditions

There are a total of 12 boundary conditions (BCs): three from the clamped end of the inboard wing, three from the free end of the outboard wing, and six from their hinged connection. They are split into two groups (Tables 1 and 2), depending on their origin.

Boundary conditions 11 and 12 follow directly from the presence of a linear torsional spring connecting the two wing segments. On the other hand, BCs 9 and 10, related to the continuity of the twist moment and shear, are less obvious. In the case of $\psi = 0$ deg, these BCs state that $\phi_1'(\ell_1, t) = \phi_2'(0, t)$ and $h_1'''(\ell_1, t) = h_2'''(0, t)$, which are the expected conditions for a single uniform beam. The presence of inertial terms in BCs 9 and 10 for the general case of $\psi = 0$ deg is related to the use of a noninertial coordinate system to describe the outboard wing [i.e., $x_2 y_2 z_2$ (see Fig. 1)].

Additional insights into the physical origins of BCs 9 and 10 are obtained from considering the case of $\psi = 90$ deg, in which case the outboard wing is perpendicular to the inboard wing. If the two wing segments are perpendicular, the elastic forces at the end of the inboard wing are balanced entirely by the inertial forces of the outboard wing. The coefficient of $\ddot{h}_1(\ell_1, t)$ in BC 9 is the moment of inertia about the y_1 axis of the outboard wing, which, after some manipulation, is given by $\frac{1}{3}m\ell_2^3 + I_y\ell_2$. The term in $\ddot{h}_1(\ell_1, t)$ corresponds to an additional twist moment that comes from the vertical motion of the line mass $\lambda_P \ell_2$ at distance x_P from the axis of rotation. These two inertial contributions balance the elastic term $GJ\phi_1'(\ell_1, t)$ in BC 9 for the case of $\psi = 90$ deg. Similarly, for BC 10 with $\psi = 90$ deg, the total mass of the outboard wing, $m\ell_2$, has a vertical acceleration of $\ddot{h}_1(\ell_1, t)$, and a mass of $\lambda_P \ell_2$ has a tangential

Table 1 Boundary conditions obtained from the definition of the problem and coordinate system

No.	Condition	Description
1	$h_1(0, t) = 0$	Zero displacement on the clamped end
2	$h_1'(0, t) = 0$	Zero bending slope on the clamped end
3	$\phi_1(0, t) = 0$	Zero deflection on the clamped end
4	$h_2(0, t) = 0$	Follows definition of $x_2 y_2 z_2$
5	$\phi_2(0, t) = 0$	Follows definition of $x_2 y_2 z_2$
6	$h_2''(\ell_2, t) = 0$	Zero bending moment on the free end
7	$h_2'''(\ell_2, t) = 0$	Zero shear at the free end
8	$\phi_2'(\ell_2, t) = 0$	Zero twist moment at the free end

Table 2 Boundary conditions extracted from Hamilton's principle

No.	Condition
9	$GJ[\phi_1'(\ell_1, t) - \phi_2'(0, t)\cos\psi] + S_y\ell_2\ddot{h}_1(\ell_1, t)\sin^2\psi$ $+[\frac{1}{3}m\ell_2^3 + I_y\ell_2]\ddot{\phi}_1(\ell_1, t)\sin^2\psi = 0$
10	$EI_{xx}[h_2'''(0, t)\cos\psi - h_1'''(\ell_1, t)] + m\ell_2\ddot{h}_1(\ell_1, t)\sin^2\psi$ $+S_y\ell_2\ddot{\phi}_1(\ell_1, t)\sin^2\psi = 0$
11	$k[h_2'(0, t) - h_1'(\ell_1, t)] - EI_{xx}h_1''(\ell_1, t) = 0$
12	$h_1''(\ell_1, t) - h_2''(0, t) = 0$

acceleration of $x_P\ddot{\phi}_1(\ell_1,t)$, both of which balance the shear from $EI_{xx}h_2'''(0,t)$.

III. Eigenvalue Evolution

This section introduces a methodology for determining the exact aeroelastic eigenvalues. The solution procedure is exact in that it solves the differential equations of motion directly. Thus, the present solution provides benchmark solutions for any discretized method of solution and it is the folding-wing analog to the Goland wing solution for a single-element beam-wing analysis. The solution procedure is also exact in that it solves for the true aeroelastic eigenvalues at all flow speeds, unlike classical flutter solution methods, which are only exact at the flutter speed.

A. Solution Procedure

The equations of motion and boundary conditions presented in the last section comprise a 12th-order system of linear, nonhomogeneous, partial differential equations with their appropriate boundary conditions. The aerodynamic lift and moment contribute only to the homogeneous problem. Even though three aerodynamic models are considered in the folding-wing model, only the solution methodology for the most sophisticated (i.e., unsteady aerodynamics) will be presented. A discussion of the variations among the different models is included in Appendix B.

In solving the aeroelastic system, the temporal eigenvalues (each denoted by $\eta^{(k)}$) and corresponding modes ($\phi_i^{(k)}$ and $h_i^{(k)}$ (are to be determined. The sought kth aeroelastic mode is assumed to follow the form

$$\phi_1^{(k)} = \sum_{j=1}^{6} C_j^{(k)} A_{1,j}^{(k)} \exp(\eta^{(k)}t + \lambda_j y_1)$$

$$\phi_2^{(k)} = \sum_{j=1}^{6} C_{j+6}^{(k)} A_{2,j}^{(k)} \exp(\eta^{(k)}t + \lambda_j y_2) - \phi_{2,p}^{(k)}$$

$$h_1^{(k)} = \sum_{j=1}^{6} C_j^{(k)} B_{1,j}^{(k)} \exp(\eta^{(k)}t + \lambda_j y_1)$$

$$h_2^{(k)} = \sum_{j=1}^{6} C_{j+6}^{(k)} B_{2,j}^{(k)} \exp(\eta^{(k)}t + \lambda_j y_2) - h_{2,p}^{(k)} \tag{17}$$

where the superscript (k) is used to denote values corresponding to the kth temporal eigenvalue, and the subscript p indicates particular solutions.

The homogeneous parts of the equations of motion in y_i for the inboard and outboard wings are identical. This homogeneous problem can be expressed as an eigenvalue problem in λ, with resulting modes of the form

$$\phi_i^{(j)} = A_{i,j}\exp(\eta t + \lambda_j y_i) \qquad h_i^{(j)} = B_{i,j}\exp(\eta t + \lambda_j y_i) \tag{18}$$

where j is used to denote the jth mode, and the subscript $i = 1, 2$ denotes, as usual, the inboard and outboard wings.

Following the solution form of Eq. (18), the homogeneous parts of Eqs. (13–16) can be expressed as

$$[M_i(\hat{\lambda})]\begin{bmatrix} A_i \\ B_i \end{bmatrix} = \begin{bmatrix} \gamma_1(\eta) & \gamma_2(\eta) + \hat{\lambda}^2 \\ \gamma_3(\eta) - \hat{\lambda} & \gamma_4(\eta) \end{bmatrix}\begin{bmatrix} A_i \\ B_i \end{bmatrix} = 0 \tag{19}$$

where

$$\begin{aligned}
\gamma_1(\eta) = \frac{1}{EI_{xx}}\bigg\{&\left(S_y - \frac{1}{8}\pi c^3 a\right)\eta^2 \\
&+ \frac{1}{2}\pi\rho_\infty c^2 U_\infty\left[\frac{1}{2} + \left(\frac{1}{2} - a\right)D(\bar{\eta})\right]\eta + \pi\rho_\infty c U_\infty^2 D(\bar{\eta})\bigg\} \\
\gamma_2(\eta) = \frac{1}{EI_{xx}}\bigg\{&\left(m + \frac{1}{4}\pi\rho_\infty c^2\right)\eta^2 + \pi\rho_\infty c U_\infty D(\bar{\eta})\eta\bigg\} \\
\gamma_3(\eta) = \frac{1}{GJ}\bigg\{&\left[I_y + \frac{1}{16}\pi\rho_\infty c^4\left(\frac{1}{8} + a^2\right)\right]\eta^2 \\
&+ \frac{1}{4}\pi\rho_\infty c^3 U_\infty\left(\frac{1}{2} - a\right)\left[\frac{1}{2} - \left(\frac{1}{2} + a\right)D(\bar{\eta})\right]\eta\bigg\} \\
&- \frac{1}{GJ}\left\{\frac{1}{2}\pi\rho_\infty c^2 U_\infty^2\left(\frac{1}{2} + a\right)D(\bar{\eta})\right\} \\
\gamma_4(\eta) = \frac{1}{GJ}\bigg\{&\left(S_y - \frac{1}{8}\pi\rho_\infty c^3 a\right)\eta^2 \\
&- \frac{1}{2}\pi\rho_\infty c^2 U_\infty\left(\frac{1}{2} + a\right)D(\bar{\eta})\eta\bigg\}
\end{aligned}$$

The expressions for γ_j are subject to change depending on the assumed aerodynamic theory; the appropriate expressions for steady and quasi-steady theories are included in Appendix B.

Equation (19) is a quadratic eigenvalue problem (QEP) in $\hat{\lambda}$, because it can be expressed as a quadratic equation in $\hat{\lambda}$ with matrix coefficients. QEPs presents various subtleties when compared with linear eigenvalue problems [12,13]. However, in practice, we can normally neglect the alluded subtleties and extract physically relevant eigenvalues from $\det[M_i(\hat{\lambda})] = 0$, neglecting any infinite eigenvalues. Three finite eigenvalues are obtained from $M_i(\hat{\lambda})$. Because the number of eigenvalues exceeds the dimensions of $M_i(\hat{\lambda})$ the eigenvectors from different eigenvalues need not be linearly independent. Having linearly dependent eigenvectors from different eigenvalues is a general characteristic of nonlinear eigenvalue problems.

If a particular eigenvalue has multiple eigenvectors that are linearly dependent, the matrix and eigenvalue are considered to be *defective*. For the current discussion, defectiveness implies that the assumed solution form $e^{\lambda y + \eta t}$ is inadequate. Solutions corresponding to defective eigenvalues will be discussed later in greater detail.

The origins and implications of defective eigenvalues for QEPs can be illustrated by considering a one-dimensional spring-mass damper. The equation of motion for this system is $\tilde{m}\,\ddot{\xi} + \tilde{c}\,\dot{\xi} + \tilde{k}\xi = 0$, and its corresponding eigenvalues are $\kappa + i\mu$ and $\kappa - i\mu$. Normally, the general solution is of the form $a_1 e^{(\kappa + i\mu)\xi} + a_2 e^{(\kappa - i\mu)\xi}$. Yet, for the case of $\mu = 0$ (i.e., $\tilde{c}^2 - 4\tilde{m}\,\tilde{k} = 0$), the eigenvalue is defective, and the general solution must be of the form $a_1 e^{\kappa\xi} + a_2 \xi e^{\kappa\xi}$.

Although only three eigenvalues are obtained from $M_i(\hat{\lambda})$, they correspond to the six eigenvalues of $M_i(\lambda)$, because $\lambda = \pm\sqrt{\hat{\lambda}}$. Additionally, an eigenvector corresponding to $\hat{\lambda}_k$ in $M_i(\hat{\lambda})$ is the same for both eigenvalues $\pm\sqrt{\hat{\lambda}_k}$ in $M_i(\lambda)$.

After obtaining the eigenvalues and eigenvectors of $M_i(\lambda)$, the nonhomogeneous problem is addressed. It is evident from Eqs. (14) and (16) that the nonhomogeneous terms do not depend on y_2. Therefore, it follows after eliminating the spatial partial derivatives in Eqs. (14) and (16) that

$$\phi_{2,p}(t) = -\phi_1(\ell_1, t)\cos\psi \qquad h_{2,p}(t) = -h_1(\ell_1, t)\cos\psi \tag{20}$$

The final step is solving another nonlinear eigenvalue problem to determine the temporal eigenvalues $\eta^{(k)}$. Once $\eta^{(k)}$ of the dynamic aeroelastic system are known, the stability problem of a folding wing can be addressed. To determine $\eta^{(k)}$, a 12 by 12 matrix $D(\eta)$ is constructed from the boundary conditions found in Tables 1 and 2 and using the solution form of Eq. (17):

$$[D(\eta^{(k)})]_{12\times 12}[C^{(k)}]_{12\times 1} = 0 \tag{21}$$

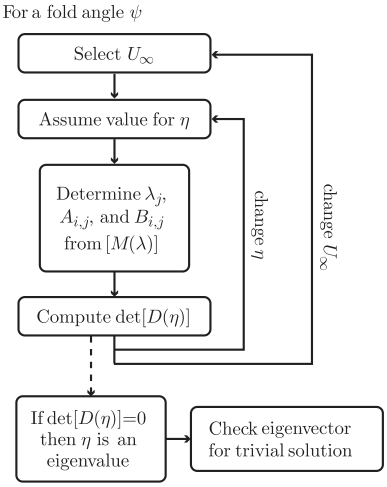

Fig. 3 Outline of numerical procedure to determine nontrivial temporal eigenvalues η as they evolve with freestream velocity U_∞.

where $\eta^{(k)}$ is the kth temporal eigenvalue, with corresponding eigenvector $C^{(k)}$.

An explicit representation of this matrix is found in Appendix C. Unlike the quadratic eigenvalue problem in Eq. (19), the current nonlinear eigenvalue problem is not a polynomial eigenvalue problem, but rather a transcendental eigenvalue problem. Therefore, there is no restriction on the number of eigenvalues that can be obtained. Once again, we can obtain all of the physically relevant solutions from the nondefective eigenvalues computed from $\det[D(\eta)] = 0$.

B. Overview of Numerical Methods

At the core of the solution procedure is an algorithm that assumes a complex value for η for a given freestream velocity and fold angle and determines whether it corresponds to a nontrivial eigenvalue. The assumed values of η are such that they sample a predetermined region of the complex plane. This procedure is repeated for different values of freestream velocity so that the evolution of aeroelastic eigenvalues can be constructed. For each assumed value of η, the solution methodology presented in the previous section is followed. Figure 3 provides an outline of the procedure. Numerical calculations for this methodology are performed in MATLAB.

The central point is that if one wishes to find the true aeroelastic eigenvalues of the system for not only the flutter point (neutrally stable) but also for damped (preflutter) as well as postflutter conditions, the present analysis is required. The standard flutter solutions methods, including V-g and p-k, do not suffice.

As shown in Fig. 3, the first step in the solution procedure is to select a fold angle and freestream velocity and to assume a value for η. Having done so, the homogeneous problem in y_i is addressed. The spatial eigenvalues λ for Eq. (19) are found using the packaged MATLAB root-finding command `roots`, which can handle complex solutions and solutions with a multiplicity greater than one. The eigenvectors corresponding to nondefective eigenvalues present no difficulty for this 2 by 2 matrix. It follows for this problem that if two or more eigenvalues are close to each other, then the matrix is possibly defective. To determine whether the eigenvalue is actually defective and not just a tightly spaced cluster of distinct eigenvalues, the *condition numbers* for the solution should be calculated [13]. This proves to be unnecessary for the current purpose, because if the eigenvalues are defective, they should be discarded because they do not follow the assumed solution. Furthermore, if they are distinct but closely spaced eigenvalues, it has been shown numerically that they correspond to trivial solutions.

After determining the λ and their appropriate eigenvectors, the particular solutions are obtained from Eq. (20). These solutions provide sufficient information to compute $\det[D(\eta)]$. It is unlikely that the assumed value for η is such that $\det[D(\eta)]$ is identically zero; therefore, multiple neighboring values of η have to considered to identify a zero crossing of both $\Re(\det[D(\eta)])$ and $\Im(\det[D(\eta)])$.

The procedure for determining zero crossings is such that $\det[D(\eta)]$ is calculated for range of $\Im(\eta)$ for a fixed $\Re(\eta)$, and zero crossings for either $\Re(\det[D(\eta)])$ or $\Im(\det[D(\eta)])$ are recorded (see Fig. 4a). Then the value of $\Re(\eta)$ is changed and the procedure is repeated. In this manner, the region of the complex η plane is sampled. The end results are contours of the surfaces corresponding to $\Re(\det[D(\eta)]) = 0$ and $\Im(\det[D(\eta)]) = 0$ at a given U_∞ (see Fig. 4b). When the contour of the $\Re(\det[D(\eta)]) = 0$ intersects that of $\Im(\det[D(\eta)]) = 0$, a possible temporal eigenvalue is identified. Finally, all of the possible eigenvalues are plotted on the complex η plane with a third axis corresponding to U_∞ (see Fig. 4c). This final 3-D plot shows the eigenvalue evolution and provides all of the information needed to identify divergence and flutter, even though it is commonly more practical to consider its real and imaginary projections.

A summary of the methodology used is depicted in Fig. 4. The progression from Fig. 4a to Fig. 4c allows for various checks on the numerical validity of the solution. Furthermore, these plots can be used to provide additional insights into the possible degeneracy of the eigenvalues. Given the nature of the nonlinear eigenvalue problem, it has been observed that special attention needs to paid to repeated eigenvalues to ensure that they are not defective. Additionally, all of the numerical results presented are limited to the *positive* $\Im(\eta)$, given that the current analysis shows a symmetry about the real axis in the η plane.

The aforementioned methodology does not address the issue of defective, trivial, and physically uninteresting solutions. As previously mentioned, defective solutions can occur when there are repeated eigenvalues, either in λ or η. If the degeneracy of an eigenvalue is greater than the number of corresponding eigenvectors,

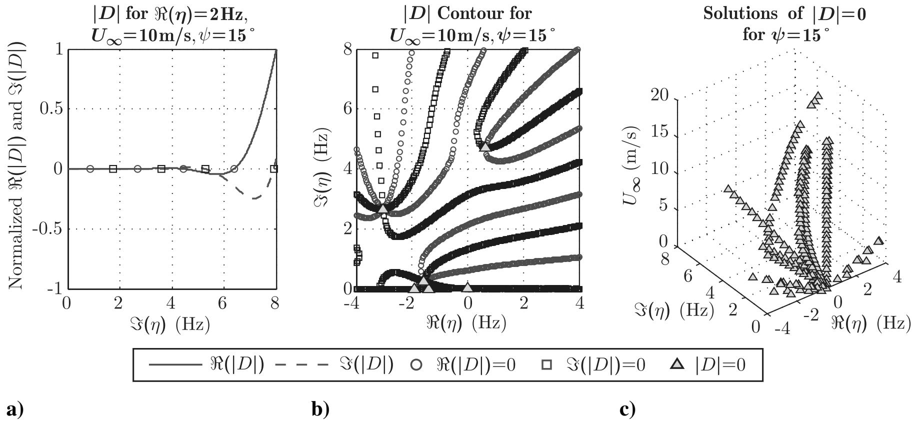

a) b) c)

Fig. 4 Sequence of numerical calculations for determining the true aeroelastic eigenvalues: a) observe zero crossings of $\Re(|D|)$ and $\Im(|D|)$, b) consider zero crossings for multiple values of $\Re(\eta)$, providing contours of $\Re(|D|) = 0$ and $\Im(|D|) = 0$ [if $\Re(|D|) = \Im(|D|) = 0$ the corresponding η is a possible eigenvalue], and c) multiple freestream velocities are considered.

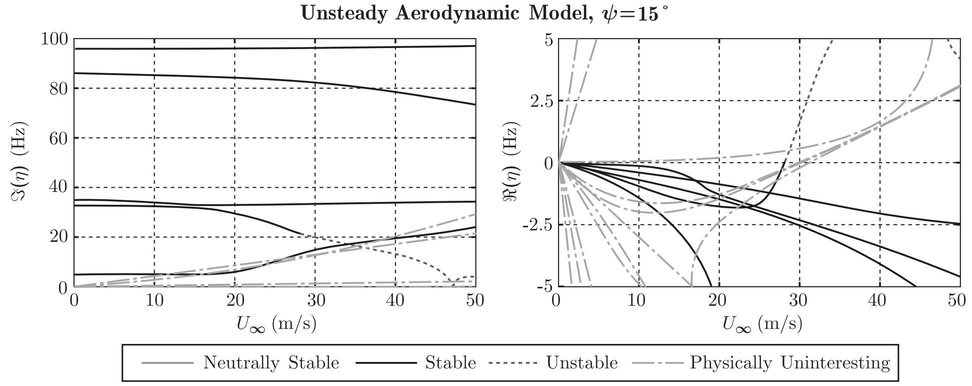

Fig. 5 Evolution of real and imaginary parts of the temporal eigenvalue η with respect to U_∞. The majority of trivial solutions occur at zero frequency, $\Im(\eta) = 0$, therefore they are depicted as single lines along the horizontal axis in the left plot. This figure should be contrasted with the two bottom plots of Fig. 6, which do not contain trivial or physically uninteresting solutions.

the eigenvalue and matrix are considered defective. A defective solution implies that a different solution form needs to be considered along with the appropriate generalized eigenvector; this issue remains a subject of investigation. Trivial and physically uninteresting solutions can be grouped together as solutions that yield zero pitch and plunge for both wing segments. Because of the limited resolution involved in sampling possible eigenvalues and numerical round-off error, it is difficult to compute eigenvectors accurately, and it is particularly challenging to identify zero quantities. When eigenvalues are suspected of leading to zero pitch and plunge, the mode shape is computed. In Table 1, there are certain locations for which ϕ_i and h_i should be identically zero; ϵ is the value of the mode shape at these locations. If the maximum amplitude of the mode shape is of the same magnitude as ϵ, the mode shape is considered to be approximately equal to zero. For nontrivial solutions, the maximum value of the mode shape is typically two or more orders of magnitude greater than ϵ. Figure 5 depicts all of the solutions, trivial and nontrivial, obtained from the model using unsteady aerodynamics. The number of trivial solutions decreases for the quasi-steady and steady models.

C. Solution Verification

Given that the current aeroelastic model for a folding-wing configuration is relatively complicated, various special cases for which the system reduces to something more familiar have been compared with known literature solutions. Each additional step of sophistication in the model has been verified with its more limited predecessor, leading all the way down to the structural model of a simple cantilevered beam. Furthermore, the special case of $\psi = 0$ deg and $k \to \infty$ is computed according to the parameters used for the Goland wing [14,15]. On a historical note, Goland's original paper [14] cites incorrect flutter speeds and frequencies for the parameters used; this mistake is corrected in the appendix of [15]. [Other classical literature (e.g., [8]) may only reference the original paper.] The flutter speed of the current model is 138.0 m/s, which is compared with 137.2 m/s of the original Goland wing. The 0.6% difference is attributed to slight differences in air density. Finally, all of the results have been compared and accurately matched to those of an independently developed component modal analysis using the same parameters.

IV. Results

A test case is considered to demonstrate the results of the model and analysis. The parameters listed in Table 3 are representative of a physical model that could be tested in the Duke University wind tunnel. As previously mentioned, the calculations culminate in a 3-D plot depicting the complex temporal eigenvalue η versus the freestream velocity U_∞. To understand this information, the imaginary and real projections of these plots for the three different aerodynamic models are depicted in Fig. 6. To avoid redundancy, only the results for positive $\Im(\eta)$ are included because the system exhibits symmetry about the $\Re(\eta)$ axis. By looking at $U_\infty = 0$, the structural natural frequencies can be read from the steady and quasi-steady models; the apparent mass terms involved in the unsteady model for this test case do not significantly change the frequencies at $U_\infty = 0$. The lowest two frequencies at $U_\infty = 0$ correspond to bending, whereas the third and fourth frequencies come from torsion.

The importance of the aerodynamic model used can be appreciated by the dramatic differences of flutter speeds and, more important, of flutter modes. The parameters for this test case were chosen such that the first torsion frequency would be slightly above a bending frequency at $U_\infty = 0$. This choice in parameters leads to the coalescence of the second bending and first torsion modes in the steady model and the early flutter instability in the quasi-steady model, which is reflected as a significant curve veering in the unsteady model.

If the first complex eigenvalue region for the steady model (which begins at the flutter speed but ends shortly thereafter) is neglected, note that the beginning of the second region in the steady model is very close to the flutter speed of the unsteady model. Even though this observation seems suggestive of a means to obtain a more accurate portrait of the actual flutter speed using the steady model, this is not consistent for different parameters, particularly for other fold angles.

Figure 7 illustrates the effects of the fold angle ψ on the flutter speed. Note that the flutter speed is not a monotonic function of fold angle and indeed has a minimum as a function of ψ. The fold angle affects both the structural and aerodynamic models, of course. But, especially for the steady flow aerodynamic model, the effects of the fold angle may be understood primarily in terms of their impact on the position of the structural natural frequencies. When the two key natural frequencies are brought closer together by a variation in fold angle, the flutter speed is lower and vice versa.

Note, moreover, that the effect of the quasi-steady or fully unsteady aerodynamic theory is to diminish the variation in flutter speed with fold angle. It is also seen that the quasi-steady aerodynamic theory gives an overly conservative prediction of flutter speed. The steady aerodynamic theory may be conservative or

Table 3 List of parameters considered for the test case

Parameter	Value
c	8.00×10^{-2} m
E	7.00×10^{10} Pa
G	2.50×10^{10} Pa
k	5.50×10^{-1} N · m
w	6.35×10^{-4} m
x_P	2.00×10^{-2} m
λ	1.50×10^{-2} m
ρ	2.70×10^{3} kg/m^3
ℓ_1	1.00×10^{-1} m
ℓ_2	1.70×10^{-1} m

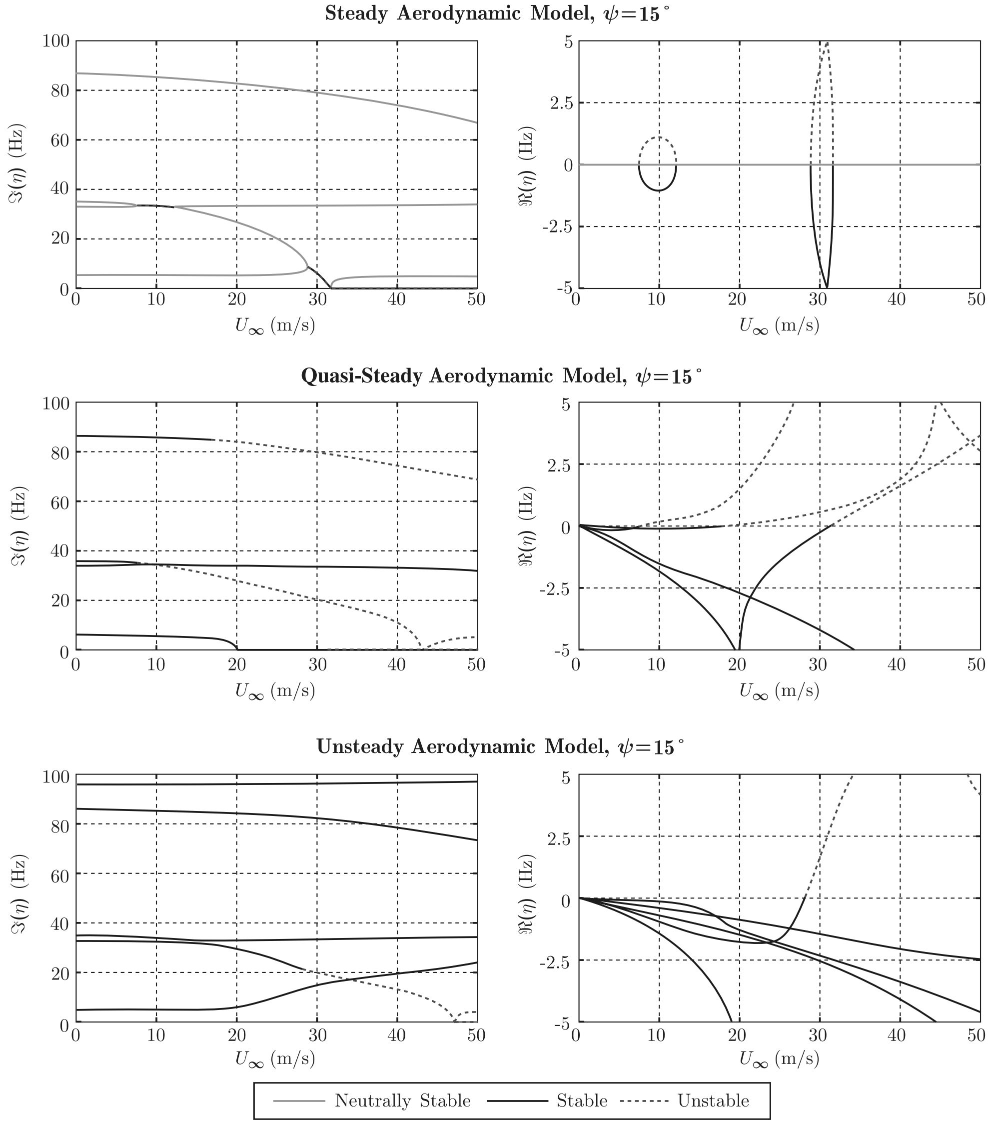

Fig. 6 Evolution of real and imaginary parts of the temporal eigenvalue η with respect to U_∞. The transition of a solid line to dashed line indicates a shift from stable to unstable oscillations. Of these transitions, the one that occurs at the lowest value of U_∞ is identified as the flutter velocity.

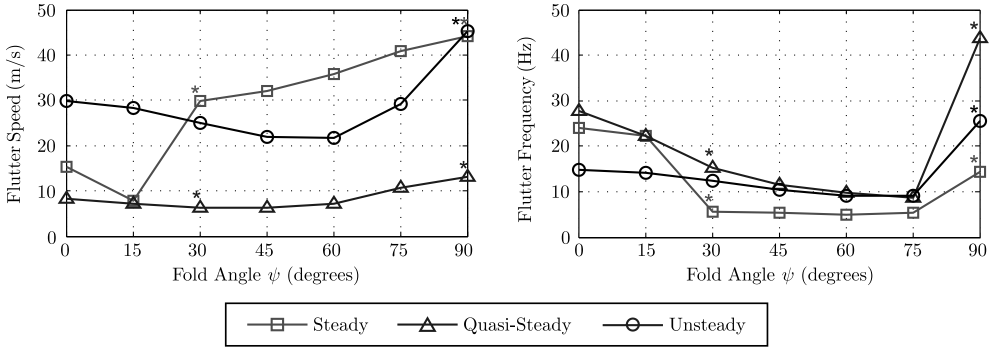

Fig. 7 Flutter speed and frequency for different fold angles. Asterisks (*) indicate changes in the flutter modes.

unconservative relative to the prediction of the fully unsteady aerodynamic theory.

V. Conclusions

A linear aeroelastic continuum model for a two-segment folding wing is developed. An exact method, free of dynamic approximations and spatial discretization, is used to determine the frequency and damping at different freestream velocities and fold angles. The detail development of the exact mathematical solution offers insight into aeroelastic phenomena before, during, and postflutter.

Solutions are obtained for the three aerodynamic models considered. The comparison of the flutter speed and mode for the three models clearly demonstrates the sensitivity of the aeroelastic behavior of folding wings to unsteady effects. Both the steady and quasi-steady models result in a change in flutter mode for a much smaller fold angle compared with the unsteady model. As one might expect, the flutter speed is initially lowered by an increase in fold angle (for the case of the more accurate unsteady model), yet the flutter does not monotonically decrease. Past a critical fold angle, the flutter speed increases beyond that of a zero fold angle.

In the special case for which the wing resembles a single cantilevered wing, the Goland wing's flutter speed and frequency are reproduced. The physical assumptions of the model should be questioned for fold angles close to 90 deg, because spanwise forces along the inboard wing, which are neglected by the current beam model, might become significant to the dynamics of the system. Regardless, exact solutions for the flutter speed and mode presented in this paper provide benchmark solutions for determining the error of approximate methods. Accurate approximate methods are unavoidable for similar aeroelastic analyses of folding-wing configurations with more complicated geometries and material properties.

Appendix A: Structural Kinetic and Potential Energy

I. Kinetic Energy

The overall kinetic energy is obtained by considering each segment separately. Furthermore, for each segment, the kinetic energy due to the homogeneous flat plate T_{iF} and the chordwise cross-sectional point mass T_{iP} are computed separately. The kinetic energy is calculated by integrating the velocity squared of differential elements of the wing. The velocity is determined with respect to a fixed coordinate system $\hat{x}\hat{y}\hat{z}$, which coincides with $x_1 y_1 z_1$ (see Fig. 1). Higher-order effects of h_i and ϕ_i are discarded to yield the desired linear model. The resulting expressions for the kinetic energy are

$$T = T_{1F} + T_{1P} + T_{2F} + T_{2P} \tag{A1}$$

$$T_{1F} = \frac{1}{24}\rho w c \int_0^{\ell_1} c^2[\dot{\phi}_1(y_1, t)]^2 + 12[\dot{h}_1(y_1, t)]^2 \,\mathrm{d}y_1 \tag{A2}$$

$$T_{1P} = \frac{1}{2}\lambda_P \int_0^{\ell_1} [x_P\dot{\phi}_1(y_1, t) + \dot{h}_1(y_1, t)]^2 \,\mathrm{d}y_1 \tag{A3}$$

$$\begin{aligned} T_{2F} = \frac{1}{24}\rho w c \int_0^{\ell_2} &(c^2 + 12y_2^2)[\dot{\phi}_1(\ell_1, t)\sin\psi]^2 \\ &+ 12[\dot{h}_1(\ell_1, t)\sin\psi]^2 + c^2[\dot{\phi}_1(\ell_1, t)\cos\psi + \dot{\phi}_2(y_2, t)]^2 \\ &+ 12[\dot{h}_1(\ell_1, t)\cos\psi + \dot{h}_2(y_2, t)]^2 \,\mathrm{d}y_2 \end{aligned} \tag{A4}$$

$$\begin{aligned} T_{2P} = \frac{1}{2}\lambda_P \int_0^{\ell_2} &y_2^2[\dot{\phi}_1(\ell_1, t)]^2 \sin^2\psi + [x_P\dot{\phi}_2(y_2, t) \\ &+ \dot{h}_2(y_2, t)]^2 \sin^2\psi + [x_P\dot{\phi}_1(\ell_1, t) + x_P\dot{\phi}_2(y_2, t)\cos\psi \\ &+ \dot{h}_1(\ell_1, t) + \dot{h}_2(y_2, t)\cos\psi]^2 \,\mathrm{d}y_2 \end{aligned} \tag{A5}$$

II. Potential Energy

The terms in the potential energy come from the deformation of the individual wing segments and from the torsional deflection between the two plates at the hinge with respect to the undeformed fold angle ψ. The contributions to the potential energy from the former and latter sources are denoted by U_{iF} and U_S, respectively. Note that there is no contribution to the potential energy of the outboard wing due to the motion of the inboard wing, and vice versa, except for that corresponding to the torsional spring connecting the two segments. Both U_{iF} and U_S follow well-known results from the literature:

$$U = U_{1F} + U_{2D} + U_S \tag{A6}$$

$$U_{iF} = \frac{1}{2}\int_0^{\ell_i} GJ[\phi_i'(y_i, t)]^2 + EI_{xx}[h_i''(y_i, t)]^2 \,\mathrm{d}y_i \tag{A7}$$

$$U_S = \tfrac{1}{2}k[h_2'(0, t) - h_1'(\ell_1, t)]^2 \tag{A8}$$

For Eqs. (A7) and (A8), Saint-Venant's rigidity constant J and the chordwise cross-sectional moment of inertia I_{xx} are[‡]

$$J = \tfrac{1}{3}w^3 c \qquad I_{xx} = \tfrac{1}{12}w^3 c \tag{A9}$$

Appendix B: Homogeneous Problem for Steady and Quasi-Steady Aerodynamic Models

The equations of motion and solution methodology discussed in the main body of this paper are based on an unsteady aerodynamic model. The aerodynamics contribute only to the homogeneous problem, particularly the definitions of $\gamma_j(\eta)$ in Eq. (19). By modifying $\gamma_j(\eta)$, any of the three aerodynamic models presently considered can be accommodated.

I. Steady Model

$$\gamma_1(\eta) = \frac{1}{EI_{xx}}\left(S_y\eta^2 + \frac{1}{2}\pi\rho_\infty c U_\infty^2\right) \qquad \gamma_2(\eta) = \frac{1}{EI_{xx}} m\eta^2$$
$$\gamma_3(\eta) = \frac{1}{GJ}\left[I_y\eta^2 - \frac{1}{2}\pi\rho_\infty c^2 U_\infty^2\left(\frac{1}{2} + a\right)\right]$$
$$\gamma_4(\eta) = \frac{1}{GJ}S_y\eta^2$$

II. Quasi-Steady Model

$$\gamma_1(\eta) = \frac{1}{EI_{xx}}\left(S_y\eta^2 + \frac{1}{2}\pi\rho_\infty c U_\infty^2\right)$$
$$\gamma_2(\eta) = \frac{1}{EI_{xx}}(m\eta^2 + \pi\rho_\infty c U_\infty \eta)$$
$$\gamma_3(\eta) = \frac{1}{GJ}\left[I_y\eta^2 - \frac{1}{2}\pi\rho_\infty c^2 U_\infty^2\left(\frac{1}{2} + a\right)\right]$$
$$\gamma_4(\eta) = \frac{1}{GJ}\left[S_y\eta^2 - \frac{1}{2}\pi\rho_\infty c^2 U_\infty\left(\frac{1}{2} + a\right)\eta\right]$$

Appendix C: Boundary Condition Matrix

The rows of the boundary condition matrix D are in the same order as the conditions found in Tables 1 and 2 following the solution form of Eq. (17).

I. For $i = 1, 2, \ldots, 6$

$$D_{1,i} = B_{1,i} \qquad D_{2,i} = \lambda_i B_{1,i} \qquad D_{3,i} = A_{1,i}$$
$$D_{4,i} = -B_{1,i}e^{\lambda_i\ell_1}\cos\psi \qquad D_{5,i} = -A_{1,i}e^{\lambda_i\ell_1}\cos\psi \qquad D_{6,i} = 0$$
$$D_{7,i} = 0 \qquad D_{8,i} = 0$$
$$\begin{aligned} D_{9,i} = &\left[GJ\lambda_i + \left(\frac{1}{3}m\ell_2^3 + I_y\ell_2\right)\eta^2\sin^2\psi\right]A_{1,i}e^{\lambda_i\ell_1} \\ &+ S_y\ell_2\eta^2 B_{1,i}e^{\lambda_i\ell_1}\sin^2\psi \end{aligned}$$
$$D_{10,i} = S_y\ell_2\eta^2 A_{1,i}e^{\lambda_i\ell_1}\sin^2\psi + (m\ell_2\eta^2\sin^2\psi - EI_{xx}\lambda_i^3)B_{1,i}e^{\lambda_i\ell_1}$$
$$D_{11,i} = -(k\lambda_i + EI_{xx}\lambda_i^2)B_{1,i}e^{\lambda_i\ell_1} \qquad D_{12,i} = \lambda_i^2 B_{1,i}e^{\lambda_i\ell_1}$$

[‡] The torsional constant J is obtain by taking the limit of $w/c \to 0$ [16].

II. For $i = 6, 7, \ldots, 12$

To obtain compact expressions, let $j = i - 6$:

$$D_{1,i} = 0 \qquad D_{2,i} = 0 \qquad D_{3,i} = 0 \qquad D_{4,i} = B_{2,j}$$

$$D_{5,i} = A_{2,j} \qquad D_{6,i} = \lambda_j^2 B_{2,j} e^{\lambda_j \ell_2} \qquad D_{7,i} = \lambda_j^3 B_{2,j} e^{\lambda_j \ell_2}$$

$$D_{8,i} = \lambda_j A_{2,j} e^{\lambda_j \ell_2} \qquad D_{9,i} = -GJ\lambda_j A_{2,j} \cos\psi$$

$$D_{10,i} = EI_{xx}\lambda_j^3 B_{2,j} \cos\psi \qquad D_{11,i} = k\lambda_j B_{2,j} \qquad D_{12,i} = -\lambda_j^2 B_{2,j}$$

Acknowledgments

This work was supported by U.S. Air Force Office of Scientific Research grant "Nonlinear High Fidelity Aeroelastic Analysis for Novel Configurations." John Schmisseur is the Program Manager. The authors thank Ivan Wang for sharing the results of his component modal analysis.

References

[1] Wlezien, R. W., Horner, G. C., McGowan, A. R., Padula, S. L., Scott, M. A., Silcox, R. J., and Simpson, J. O., "The Aircraft Morphing Program," 39th AIAA/ASME/ASCE/AHS/ASC Structures, Structural Dynamics, and Materials Conference and Exhibit, Long Beach, CA, AIAA, 2005, pp. 1–13.

[2] Wilson, J. R., "Morphing UAVs Change the Shape of Warfare," *Aerospace America*, Vol. 42, No. 2, 2004, pp. 28–29.

[3] Lee, D. H., and Weisshaar, T. A., "Aeroelastic Studies on a Folding Wing Configuration," 46th AIAA/ASME/ASCE/AHS/ASC Structures, Structural Dynamics and Materials Conference, Austin, TX, AIAA, 1998.

[4] Radclie, T. O., and Cesnik, C. E. S., "Aeroelastic Response of Multi-Segmented Hinged Wings," 42nd Structures, Structural Dynamics, and Material Conference, Seattle, WA, AIAA Paper 2001-1371, April 2001.

[5] Radcliffe, T. O., and Cesnik, C. E. S., "Aeroelastic Behavior of Multi-Hinged Wings," *CEAS International Forum on Aeroelasticity and Structural Dynamics*, Madrid, 5–7 June 2001, pp. 449–459.

[6] Fung, Y. C., *An Introduction to the Theory of Aeroelasticity*, Dover, Mineola, NY, 2002, pp. 30–36.

[7] Dowell, E. H., Clark, R., Cox, D., Curtiss, H. C., Edwards, J. W., Hall, K. C., Peters, D. A., Scanlan, E. S., Sisto, F., and Strganac, T. W., *A Modern Course in Aeroelasticity*, 4th ed., Kluwer Academic, Dordrecht, The Netherlands, 2004, pp. 87–95.

[8] Bisplinghoff, R. L., Ashley, H., and Halfman, R., *Aeroelasticity*, Dover, Mineola, NY, 1996, pp. 251–281.

[9] Edwards, J. W., and Wieseman, C. D., "Flutter and Divergence Analysis Using the Generalized Aeroelastic Analysis Method," *Journal of Aircraft*, Vol. 45, No. 3, 2008, pp. 906–915. doi:10.2514/1.30078

[10] Peters, D. A., "Two-Dimensional Incompressible Unsteady Airfoil Theory—An Overview," *Journal of Fluids and Structures*, Vol. 24, No. 3, 2008, pp. 295–312. doi:10.1016/j.jfluidstructs.2007.09.001

[11] Theodorsen, T., "General Theory of Aerodynamic Instability and the Mechanism of Flutter," NACA Rept. 496, 1935.

[12] Lancaster, P., and Tismenetsky, M., *The Theory of Matrices with Application*, 2nd ed., Academic Press, San Diego, CA, 1985, pp. 126–131.

[13] Tisseur, F., and Meerbergen, K., "The Quadratic Eigenvalue Problem," *SIAM Review*, Vol. 43, No. 2, 2001, pp. 235–286. doi:10.1137/S0036144500381988

[14] Goland, M., "The Flutter of a Uniform Cantilever Wing," *Journal of Applied Mechanics*, Vol. 12, No. 4, 1945, pp. 197–208.

[15] Goland, M., and Luke, Y. L., "The Flutter of a Uniform Cantilever Wing with Tip Weights," *Journal of Applied Mechanics*, Vol. 15, No. 1, Mar. 1948, pp. 13–20.

[16] Timoshenko, S. P., and Goodier, J. N., *Theory of Elasticity*, McGraw–Hill, New York, 1970, pp. 245–249.

C. Cesnik
Associate Editor